

Compressed SUSY searches with Monojet events at CMS

Robyn Elizabeth Lucas
Imperial College London

A dissertation submitted to Imperial College London
for the degree of Doctor of Philosophy

Abstract

This is the abstract, find me in frontmatter.tex

Declaration

This dissertation is the result of my own work, except where explicit reference is made to the work of others, and has not been submitted for another qualification to this or any other university. This dissertation does not exceed the word limit for the respective Degree Committee.

Robyn Lucas

Acknowledgements

Mr Darcy and Mr Merlin deserve particular thanks.

Preface

This thesis describes my research on various aspects of the CMS particle physics program, centred around the CMS detector and LHC accelerator at CERN in Geneva.

For this example, I'll just mention Chapter ?? and Chapter ??.

Contents

1. Introduction	2
2. Theory and Motivations	3
2.1. The Standard Model of Particle Physics	4
2.1.1. Gauge Symmetries	4
2.1.2. Electroweak Symmetry Breaking	4
2.2. Motivation for Physics Beyond the Standard Model	4
2.3. Supersymmetry	4
2.3.1. Compressed Supersymmetry	4
3. The LHC and CMS experiment	5
3.1. The LHC	5
3.2. The CMS Detector	7
3.2.1. The Tracking System	9
3.2.2. The Electromagnetic Calorimeter	10
3.2.3. The Hadronic Calorimeter	11
3.2.4. The Muon System	13
3.3. Event Reconstruction	14
3.3.1. Jets	15
3.3.2. Missing Transverse Energy	17
3.3.3. Muons	19
3.4. The Trigger	21
3.4.1. The L1 Trigger	22
3.4.2. The High Level Trigger	24
4. Jet Algorithms for the L1 Trigger Upgrade	25
4.0.3. ALGORITHMS FOR L1 JET RECONSTRUCTION	25
4.0.4. UPGRADE L1 JET ALGORITHM PERFORMANCE	28

5. Searching for Compressed SUSY with monojet events	31
5.1. Analysis	31
A. Pointless extras	32
A.1. Like, duh	32
A.2. $y = \alpha x^2$	32
Bibliography	34
List of Figures	36
List of Tables	39
1. Acronyms	39

“For Peter”

—

Chapter 1.

Introduction

“Everything starts somewhere, although many physicists disagree.”

— Terry Pratchett

Chapter 2.

Theory and Motivations

“Absence of evidence is not evidence of absence.”

— Carl Sagan, 1934 - 1996

The Standard Model (SM) of particle physics provides a fabulously accurate description of the most fundamental forces and particles known to exist. It has been shown to be robust beyond measure in the first years of running at the LHC. In this chapter I discuss the theory of the SM, its successes and failings, and motivate a Supersymmetric extension of the SM.

2.1. The Standard Model of Particle Physics

2.1.1. Gauge Symmetries

2.1.2. Electroweak Symmetry Breaking

2.2. Motivation for Physics Beyond the Standard Model

2.3. Supersymmetry

2.3.1. Compressed Supersymmetry

Chapter 3.

The LHC and CMS experiment

“Insanity: doing the same thing over and over again and expecting different results.”

— Albert Einstein, 1879 - 1955

Probing the physics of the Standard Model (SM) and beyond at the TeV scale is only possible with the technologically unparalleled apparatus situated at the European Organisation for Nuclear Research (CERN). This chapter will introduce the hugely complex machinery of the LHC, which provides proton-proton collisions at energies in excess of $\sqrt{7}$ TeV, and outline the main features of the Compact Muon Solenoid (CMS) experiment, of which the author is a member, with particular focus on those features relevant to the material presented in this thesis. Section 3.1 presents the main features of the Large Hadron Collider (LHC), and Section 3.2 provides an overview of the CMS detector. Object reconstruction is described in Section 3.3 and the CMS trigger is discussed in Section 3.4.

3.1. The LHC

The LHC is the world’s largest and most energetic synchrotron particle collider. Housed in the tunnel built for the Large Electron-Positron Collider (LEP) collider that operated during the 1990’s at CERN, the LHC is a double ring circular collider 27 km in circumference, and sits on the bedrock beneath the Franco-Swiss border, close to Geneva,

Switzerland. It is designed for both proton-proton (pp) and heavy ion (PbPb) collisions at a centre of mass energy $\sqrt{s} = 14$ TeV and luminosity of $10^{34} \text{cm}^{-2} \text{s}^{-1}$.

Currently the world's only operating collider able to study physics at the TeV scale, the LHC consists of thousands of superconducting magnets which act to accelerate, bend and focus two beams of protons (or heavy ions) that circulate in opposite directions around the accelerator. A chain of accelerators, shown in Figure 3.1 and culminating with the Super Proton Synchrotron (SPS), inject bunches of approximately one hundred billion protons 25 or 50 ns apart at $\sqrt{s} = 450$ GeV into the two beams of LHC. Oscillating electric fields provided by 1232 superconducting dipole magnets act to accelerate the beams up to the operating centre of mass energy, which for the data used in this thesis was $\sqrt{s} = 8$ TeV, with bunch crossings every 50 ns. Once protons are accelerated to the operational \sqrt{s} , the LHC acts as a storage ring, and collisions can occur. Either side of four points around the LHC ring, very high precision magnetic fields, provided by quadrupole and higher order multipole magnets, position and focus the beams such that each bunch has a diameter of $16 \mu\text{m}$. The chance of a pp collision with large momentum transfer at the four interaction points around the LHC ring is thereby increased, and the number of such collisions per bunch crossing, termed pile-up (PU) for the data used in this thesis was ~ 20 .

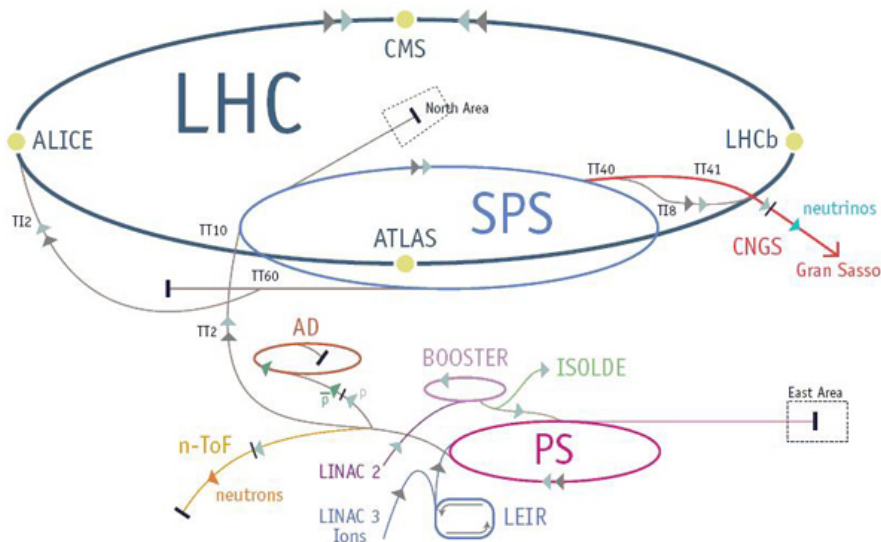


Figure 3.1.: The LHC accelerator ring, showing the locations of the four main experiments at the four collision points.

Interaction points are at the centre of four large particle detectors, shown in Figure 3.1: A Large Ion Collider Experiment (ALICE) [1], A Large Toroidal LHC ApparatuS

(ATLAS) [2], Compact Muon Solenoid (CMS) [3] and Large Hadron Collider Beauty (LHCb) [4]. They act to identify particles produced as a result of a pp or PbPb bunch crossing through a combination of tracking and calorimetry, in order to reconstruct and measure physical processes, to test currently accepted theories and search for new physics.

3.2. The CMS Detector

The CMS detector is a general purpose particle detector situated at Point 5 on the LHC ring, designed to carry out many different measurements for various physics goals. Close to 4π reconstruction with efficient particle identification and reconstruction allows measurements of photons, muons, electrons, taus, hadronic showers and missing transverse momentum. A diagram of CMS is shown in Figure 3.2. It is 21.6 m long, 14.6 m in diameter and weighs 12500 T. It consists of different sub-detectors, each of which measures a different particle or property, and is built around a central 12.5 m long 4 T superconducting solenoid magnet and its iron return yoke. CMS consists of a barrel region, containing the solenoid, and endcaps to extend the forward and backward coverage.

The different sub-detectors are arranged in an onion structure. Closest to the beam line is the silicon tracking system. A very highly resolution pixel detector lies closest to the interaction region, followed by a granular strip detector. Charged particle momenta measurements are made using the curvature of tracks in the uniform magnetic field provided by the solenoid, as well as measurements of displaced vertices and impact parameters which are essential for identifying heavy flavor decays. Energy measurements are provided by the calorimeters, which lie outside of the tracker; the Electromagnetic Calorimeter (ECAL) and Hadronic Calorimeter (HCAL). The highly granular ECAL consists of 70,000 transparent lead tungstate crystals. As electrons and photons pass through, they cause electromagnetic showers in the crystals, which produce scintillation light. The sampling HCAL consists of slabs of brass interleaved with plastic. Incident hadrons shower when passing through the absorber (brass), causing scintillation light to be produced in the active material (plastic) as the shower passes through. Scintillation light produced in the crystals, or plastic, is collected by photodetectors and used to infer the incident particle energy and position. The solenoid lies outside of the HCAL and provides a 3.8 T axial magnetic field. Embedded in the iron return yoke of the magnet sits the muon system. Three different types of muon detectors are used to identify muons

and make momentum and charge measurements over a large kinematic range. More information on the CMS detector can be found in Ref. [3].

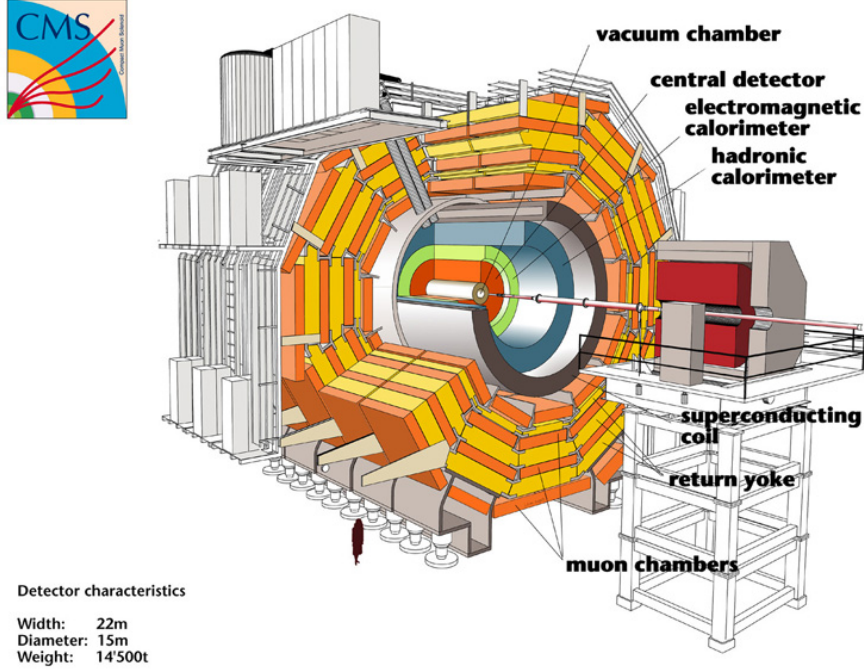


Figure 3.2.: The CMS detector, with the main subsystems labelled.

CMS uses a right-handed coordinate system: the x -axis points south towards the centre of the LHC ring, the y -axis points vertically upwards and the z -axis is in the direction of the beam, where positive z is to the west. More useful is the cylindrical coordinate system, defined in terms of r , ϕ and θ . The azimuthal angle ϕ is measured from the x -axis in the xy plane, where the radial component is denoted r . The polar angle θ is defined in the rz plane, and the pseudorapidity

$$\eta = -\ln \tan(\theta/2). \quad (3.1)$$

Convention is that the position of a particle is described in terms of η and ϕ , where $\eta = 0$ is along the y -axis and $\eta = \infty$ is along the beam direction; and $-\pi < \phi < \pi$. The distance between particles is commonly described in terms of the variable $\Delta R = \sqrt{\Delta\phi^2 + \Delta\eta^2}$.

The LHC is a hadron collider, and as such, collides non-fundamental particles. Inelastic collisions with large momentum transfer can occur between component quarks and gluons, however in a single bunch crossing there will also be many low energy, elastic, soft scatters, as well as the remnant part of any protons that have had a hard collision. As a result, the forward and backward directions are highly radiative environments and therefore difficult

to instrument due to high occupancy and radiation damage. CMS has endcaps to extend the detector coverage at high η , however it is not possible to reconstruct momentum of a single interaction in the direction of the beam. Additionally, interesting physics is a result of a hard collision, where energy is available for the creation of new particles. It can be characterized by the amount of energy in the transverse (xy) plane. For these reasons, particle energy and momenta are described only in the transverse plane, where conservation laws can be applied. By conserving energy and momentum in the transverse plane, any imbalance can be assigned to a particle leaving the detector without any trace; for example from a neutrino, or, from new physics processes such as Dark Matter (DM) production. 4π particle reconstruction and measurements of missing transverse energy, the ‘tell-tale’ sign of new physics, makes CMS perfectly suited to searching for physics beyond the SM.

3.2.1. The Tracking System

The tracker is designed for precise and efficient measurement of charged particle trajectories (and therefore position and momentum) as they emerge from the interaction point. Additionally, reconstruction of any secondary vertices is crucial for identifying heavy flavor decays such as jets that originate from b-quarks.

The LHC provides bunch crossings every 25 or 50 ns, resulting in ~ 20 pp interactions, giving rise to of order 1000 particles. All of these traverse the tracker. The granularity of the tracker must be such that one can determine which of the ~ 20 pp vertices each of the particles come from, and the electronics fast enough that the information is sent on in time for the next bunch crossing to arrive. With such high particle fluxes, the tracker is also subject to a huge amount of radiation damage. These conditions must be dealt with using the least amount of material possible in order to limit multiple scattering, photon conversion, bremsstrahlung and nuclear interactions. To meet with such criteria, and to have an estimated lifetime of 10 years, the tracker is constructed entirely from silicon.

The tracker consists of an all silicon pixel and strip detector. Measuring 5.8 m in length and 2.5 m in diameter, with a total active area of 200 m², it surrounds the interaction region. The pixel detector has three layers in the barrel, at radii of 4.4 cm, 7.3 cm and 10.2 cm. In the endcaps, there are two disks at distances $z = \pm 34.5, \pm 46.5$ cm. The strip detector has a length of 5.8 m and a diameter of 2.4 m, and is composed of four subsystems: the Tracker Inner Barrel (TIB), Tracker Outer Barrel (TOB), Tracker

Inner Disks (TID) and Tracker Endcaps (TEC). The CMS tracker geometry is shown in Figure 3.3.

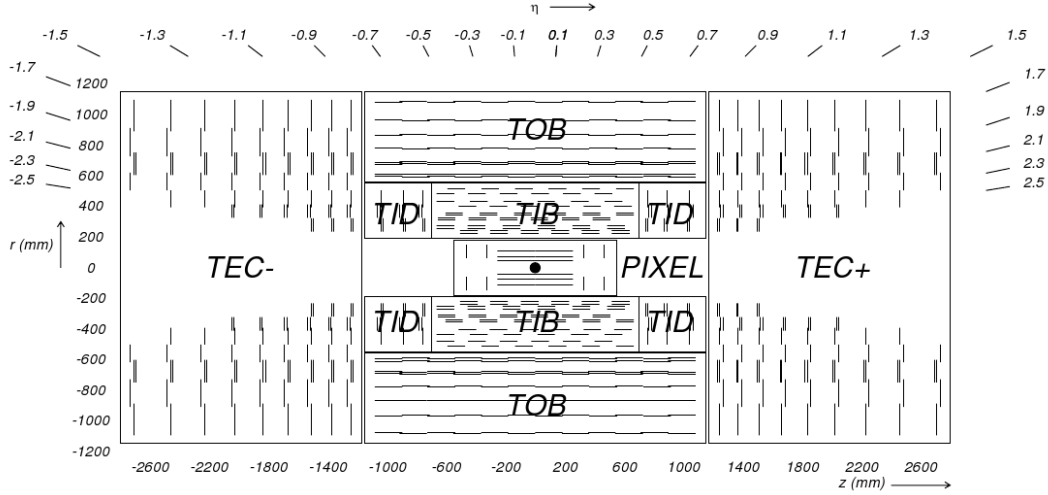


Figure 3.3.: The CMS tracker, shown in the rz plane. The pixel detector is shown at the centre of the tracker, closest to the interaction region (shown by the black dot), and the strip detector surrounds it. The different subsystems of the strip detector are shown, taken from Ref. [3].

3.2.2. The Electromagnetic Calorimeter

High resolution photon and electron position and energy measurements are provided by the lead tungstate (PbWO_4) crystal ECAL, which covers pseudorapidity up to $|\eta| < 3$. It is made up of the Electromagnetic Calorimeter Barrel (EB), covering the range $0 < |\eta| < 1.479$, and the Electromagnetic Calorimeter Endcap (EE), covering the range $1.479 < |\eta| < 3$.

Both fast response times (80% of scintillation light is emitted in 25 ns) and radiation hardness are required from the ECAL, motivating the choice of material. In addition, it is very dense (8.28 g cm^{-3}), has a short radiation length ($X_0 = 0.89 \text{ cm}$), and small Molière radius (2.2 cm), making it well suited to a compact, fine granularity calorimeter. 61,200 crystals in the barrel and 7,324 crystals in the endcaps are tapered in shape and arranged in a quasi-projective geometry, angled at 3° to ensure that particle trajectories avoid cracks between them. Barrel crystals have a front face of $22 \times 22 \text{ mm}^2$ and a length of 23 cm, corresponding to $25.8 X_0$. Endcap crystals have a front face of $28.6 \times 28.6 \text{ mm}^2$ and length corresponding to $24.7 X_0$. Electromagnetic showers are therefore expected to be contained within one crystal length, so only a single layer of crystals is needed.

A preshower detector is placed in front of the endcaps, with a thickness of $3X_0$, in the range $1.653 < |\eta| < 2.6$, in order to distinguish between single photons and photon pairs resulting from neutral pion decay. The ECAL geometry is shown in Figure 3.4.

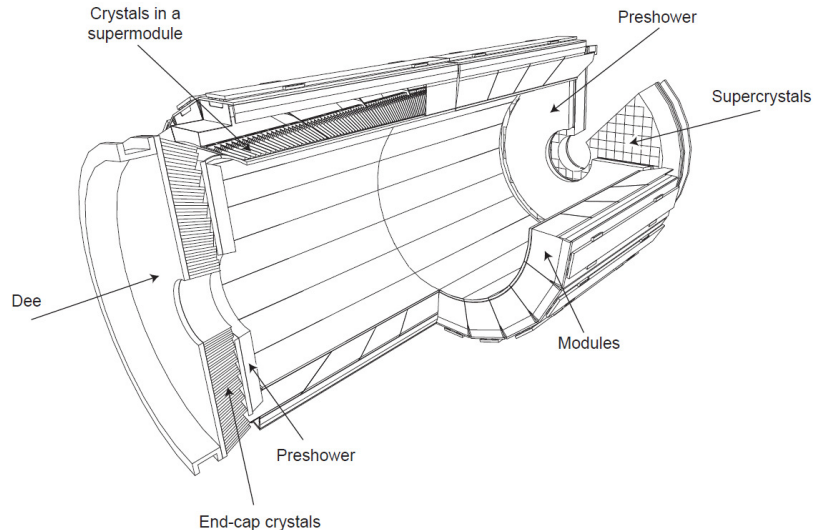


Figure 3.4.: Geometric view of the CMS ECAL. Barrel crystals are arranged in modules and supermodules, and endcap crystals arranged in supercrystals. Also shown is the preshower detector.

The very dense material PbWO_4 causes incident photons and electrons to shower. Resulting pair produced electrons and positrons, and radiated photons, cause scintillation light in the transparent, polished crystals. The amount of light produced is proportional to the incident particle energy, and is collected by an Avalanche Photo-Diode (APD) on the end of each crystal in the barrel, and a Vacuum Photo-Triode (VPT) in the endcaps. These photodetectors also have to be radiation hard and operate successfully in the 3.8 T magnetic field, while providing significant amplification to signal. Both the crystal and photodetector performance has a strong temperature dependence, so the ECAL is kept at a constant temperature of 18° via a water cooling system, and is stable to $\pm 0.05^\circ \text{C}$.

3.2.3. The Hadronic Calorimeter

The HCAL provides complementary energy measurements of hadronic showers, crucial for measuring jets and missing transverse energy. It is a sampling brass calorimeter, built from alternating layers of large, absorbing brass plates, interleaved with scintillating plastic tiles arranged in trays. Sitting within the bore of the solenoid, the Hadron

Barrel (HB) covers pseudorapidity $|\eta| < 1.3$, and the Hadron Endcaps (HE) on each side enclose $1.3 < |\eta| < 3$. To attain a most hermetic detector, there is also a Hadron Forward (HF), which extends coverage right up to $|\eta| < 5.2$.

The quality of the HCAL's measurements is dictated by the fraction of the hadronic shower that passes through the scintillator; the plastic must be thick enough to catch the majority of the shower. This demand for radial extension is at odds with the location of the HCAL, from the outer edge of the ECAL at $r = 1.77$ m, and the inner edge of the solenoid at $r = 2.95$ m. Providing a compromise, an outer hadronic calorimeter, Hadron Outer (HO), is placed outside of the vacuum tank of the magnet and supplements the HB. Using the solenoid coil as absorber material, it can identify late starting showers, providing sufficient containment for 11.8 interaction lengths (λ_L). Five rings of HO are arranged along the z -axis of the detector, where the central ring at $\eta = 0$ has two layers at $r = 3.82$ m and 4.07 m, and the rest have a single layer at $r = 4.07$ m. Figure 3.5 shows the geometry of the HCAL.

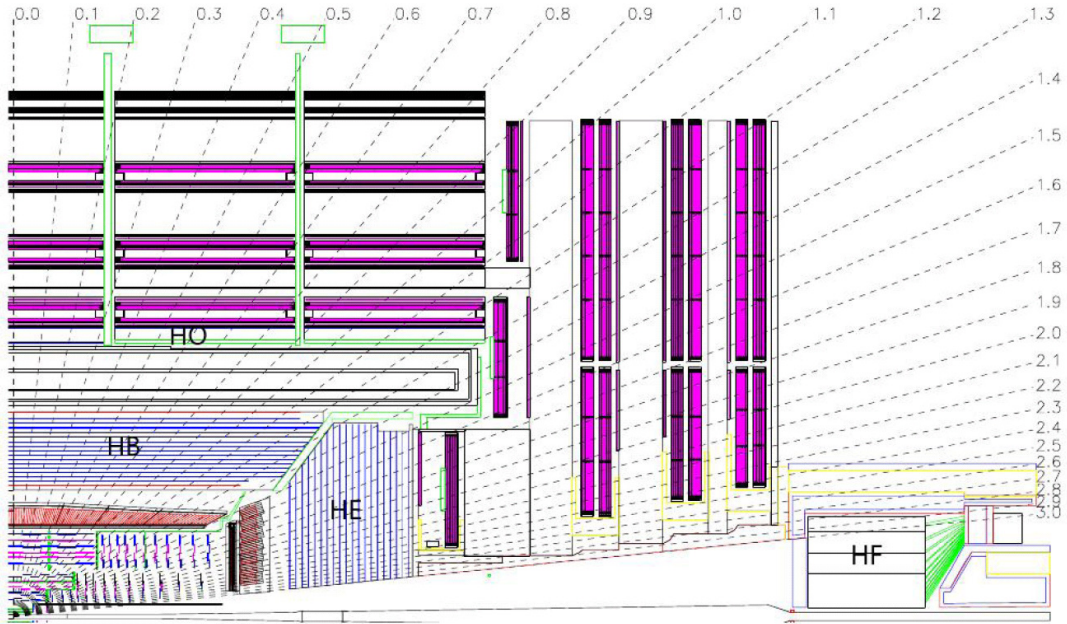


Figure 3.5.: Longitudinal view of the CMS HCAL. Locations of the HB, HO, HE and HF are shown with values of η . The purple regions represent the muon detectors which further restrict the volume of the HO.

Hadron showers are created in the brass absorber plates, through nuclear interactions in the material, and the plastic scintillator tiles produce blue-violet light when the shower passes through. It is read out using wavelength shifting fibres, sending the now green light down transparent fibres to Hybrid Photodetectors (HPD) which produce an electrical

signal proportional to the incident hadron energy. The first layer of plastic tiles are placed in front of the first absorber plate in order to sample the incoming shower as it develops in the material between the ECAL and the HCAL. The final layer of scintillator placed after the final brass plate to catch any late developing showers. There are 70,000 plastic scintillator tiles in the HB and 20,916 tiles in the HE.

The HF uses a different technology in order to cope with the much harsher environment in which it is situated. With an average energy of 760 GeV deposited in the HF per pp collision at LHC design energy, peaking at the highest rapidity point closest to the beam line, radiation hardness and occupancy requirements demand alternative materials. Steel absorber plates are embedded with scintillating quartz fibres, which act to detect the Cherenkov light emitted by charged particles in the shower. It is therefore most sensitive to the electromagnetic component of the shower.

3.2.4. The Muon System

Muons are a powerful tool for recognising signs of interesting physics. A relatively easy experimental signature to identify, muons can provide excellent 2- or 4-particle mass resolutions as they do not suffer from radiative losses (as electrons do). Muon reconstruction is therefore a central design feature. Embedded in the iron flux-return yoke of the solenoid, the muon system combines three methods of gaseous detection to identify, carry out high resolution momentum measurements, and trigger events, up to $|\eta| < 2.4$.

In the barrel ($|\eta| < 0.9$), magnetic flux is concentrated in the iron return yoke so the residual field is very small. There is also a low muon rate and neutron induced background, so Drift Tube (DT) chambers are used. In the endcaps ($0.9 < |\eta| < 2.4$), magnetic field and muon rate are much higher, so Cathode Stripe Chambers (CSCs) are used instead; they have a faster response time, higher granularity and better radiation hardness. Both the DT and CSCs have excellent position resolution. An additional system of Resistive Plate Chambers (RPCs) in both the barrel and endcaps provide an independent signal which has good time resolution (and poorer position resolution) and serves as a trigger.

By combining information from the tracker, and from either the DT or CSCs and RPCs, CMS has excellent muon reconstruction. Precise momentum resolution is achieved for the whole kinematic range, from 10 GeV to > 500 GeV, shown in Figure 3.6.

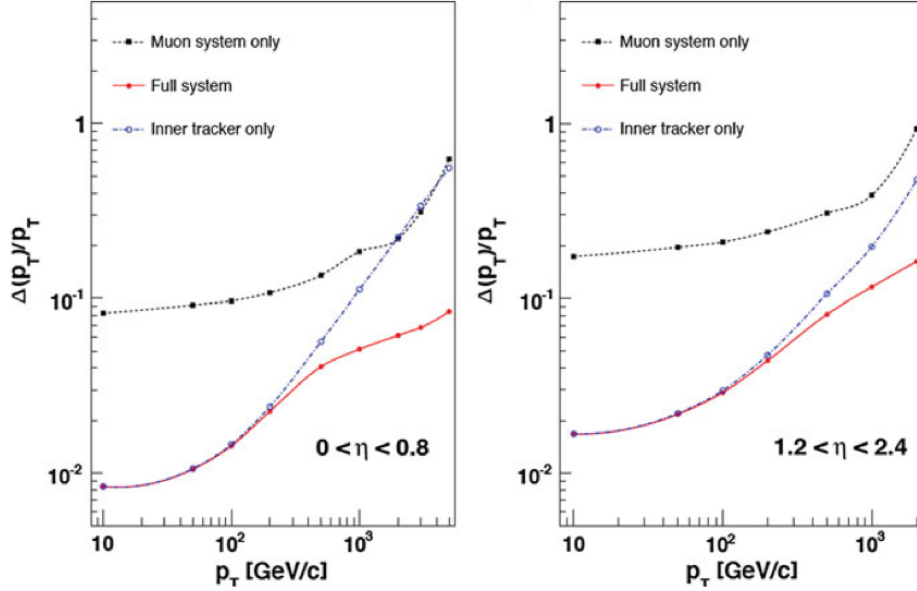


Figure 3.6.: Muon transverse momentum resolution, shown as a function of muon p_T in the barrel (left) and the endcaps (right). The resolution of the tracker and muon system is shown, and the enhancement gained by combining the information.

3.3. Event Reconstruction

It is by piecing together the information from the various subsystems of the CMS detector that, for example, a track in the tracking system, or an energy deposit in the HCAL, can be attributed to a particle or “physics object”. Figure 3.7 shows a slice of the whole detector with each of the main physics objects traversing it: muons, electrons, photons, and charged and neutral hadrons. Each of these leaves a different signature. Charged particles leave tracks in the silicon tracker, curved under the influence of the magnetic field. Electrons and photons cause electromagnetic showers, leaving energy deposits in the ECAL. Hadrons penetrate further, showering and leaving energy deposits in the HCAL. Muons are the only visible particles to reach the muon system, where they leave tracks.

Particles can then be identified by combining tracking information with data from the calorimeters and muon system. If there is an energy deposit in the ECAL, the only way to distinguish between a photon or electron is by looking to see if there are hits in the tracker, leading to the position of the electromagnetic shower in the calorimeter. Similarly, the momentum measurement of the electron, determined using the curvature of the track it leaves (also used to reconstruct its charge), can be combined with the

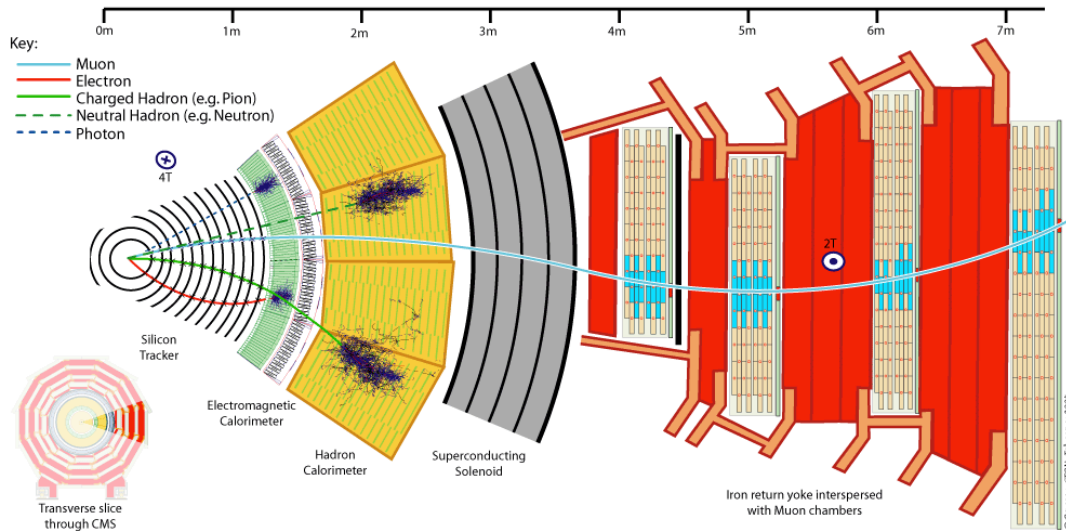


Figure 3.7.: A slice of the CMS detector is shown, with various particles, or physics objects, traversing it. By combining information from each of the subdetectors, each of the particles produced in an event can be identified and the whole event reconstructed.

energy measurement made using the amount of scintillation light produced in the ECAL to get a better resolution. If there is no track leading to the electromagnetic shower, a photon is instead reconstructed. Hadronic showers in the HCAL due to charged and neutral incident hadrons can also be distinguished by their tracks. A muon will leave the tell-tale sign of hits in the tracker, and hits in the outer muon chambers, where position, momentum and charge measurements from both ensure the initial track in the silicon tracker matches up to the track in the muon system. Dual measurements also lead to enhanced resolution.

Below is a summary of the object reconstruction most relevant to the physics analysis described in Chapter 5. More information can be found in Ref. [5].

3.3.1. Jets

Copious numbers of quarks and gluons are produced during pp collisions in CMS, a consequence of the huge Quantum Chromo-Dynamics (QCD) cross section. Through the strong interaction they fragment and immediately hadronize, and a spray of hadrons is produced in the direction of an initial quark or gluon. Various algorithms have been developed in order to group the spray of hadrons into a “jet”, and assign an energy, direction and transverse momentum to it.

In the analysis presented in this thesis (and in general at CMS), the anti- k_T algorithm [6] is used with a distance parameter, $R = 0.5$. It behaves like an idealised cone algorithm, using a distance parameter to cluster particles into cone shapes, with a radius R . Soft particles are clustered with nearby hard particles rather than with themselves, leading to conical jets, which - crucially - are resilient to soft radiation on the boundary of the cone. Likewise, the area of the jet is unaffected by soft radiation on the boundary, and is equal to πR^2 . These features make the anti- k_T algorithm the preferential jet algorithm at CMS, due to its insensitivity to soft radiation that arises from sources such as PU; see Figure 3.8.

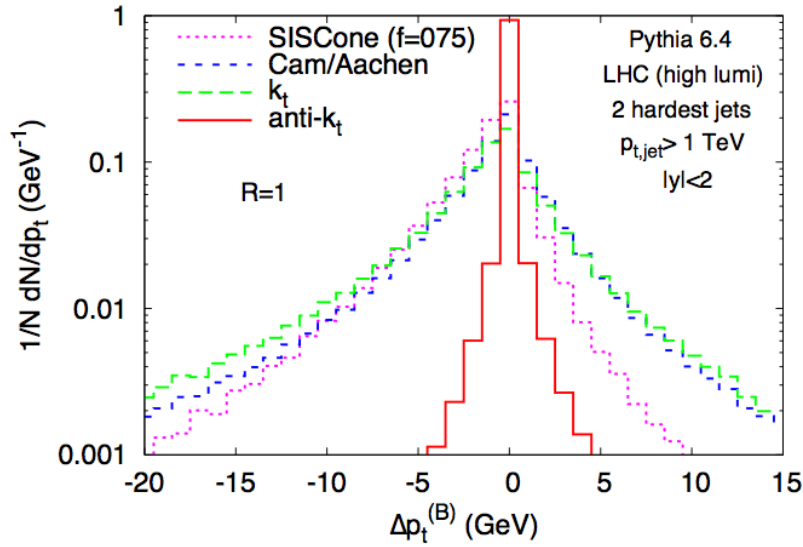


Figure 3.8.: The relative insensitivity of the anti- k_T algorithm to PU is shown, compared to other common jet algorithms. The distribution of back reaction, corresponding to the net change in p_T to each of the two hardest jets (where each jet has $p_T > 200$ GeV), when adding $PU \sim 25$ to the event, corresponding to LHC running conditions in the next phase of data taking starting in 2015. Taken from [6].

Several types of jets exist at CMS, in which the anti- k_T algorithm is given different inputs. Calorimeter (Calo) jets use information from the calorimeter only. ECAL crystals are grouped in 5×5 arrays into “towers”, which measure 0.087×0.87 in $\Delta\phi \times \Delta\eta$ space (in the barrel region) and are matched to aligning blocks of HCAL. The sum of the energy deposits in both layers of calorimeter are used as inputs to the jet algorithm, where towers are treated as massless and an η dependent energy threshold has been placed on each tower to reduce the effect of instrumental noise.

The Particle Flow (PF) algorithm [7] creates a list of all stable particles in an event: photons, electrons, muons, neutral hadrons and charged hadrons. Particle momentum, direction and type are determined using all of the subdetectors of CMS, which, with its silicon tracker, highly granular ECAL and strong magnetic field is ideally suited to the task. The reconstruction of the fundamental constituents of a typical jet - largely photons, charged hadrons and neutral hadrons - uses charged particle tracks and calorimeter clusters, termed “elements”. A traversing particle is expected to give rise to one, or several elements arising from separate subdetectors. To reconstruct a particle, these elements are therefore grouped into “blocks”: links of one, two or three elements that have arisen due to the same object. Blocks can then be interpreted as individual particles, and the resulting list of reconstructed particle flow particles gives a global description of each event. This list of particles is used as the input to the anti- k_T algorithm, producing PF anti- k_T jets.

The energy of a typical jet consists of energy from charged particles (65%), photons (25%) and neutral hadrons (10%). Therefore, typically, 90% of the jet energy can be reconstructed with good precision, utilising measurements from the high resolution silicon tracker. Only 10% of the energy is reconstructed using the relatively poor resolution hadron calorimeter, and with calibration corrections of order 10-20%. Therefore, PF jets, made of reconstructed particles, are much closer to jets made of simulated, Monte Carlo (MC) generated particles than those that rely just on calorimeter information alone (such as Calo jets), see Figure 3.9. PF jets consequently have excellent position and energy resolution. Jet momentum resolution, defined as the ratio $(p_T^{\text{rec}} - p_T^{\text{gen}})/p_T^{\text{gen}}$, (where “rec” is for reconstructed, i.e. PF or Calo jets, and “gen” is for jets taken from simulation) is shown in Figure 3.10. It is because of the excellent performance of the PF algorithm, as input to the anti- k_T that it is used most commonly across CMS analyses, including in the analysis presented in this thesis.

3.3.2. Missing Transverse Energy

As discussed in the previous sections, CMS is hermetic, has coverage up to $|\eta| = 5$ and excellent particle reconstruction; a very complete picture of each event is available. As such, is it very well suited to make measurements of weakly interacting particles, such as neutrinos, that do not leave any trace within any subsystem of the detector; and are only evident through an imbalance of transverse momentum. New physics processes, such as R-parity conserving SuperSYmmetry (SUSY), would also lead to signatures

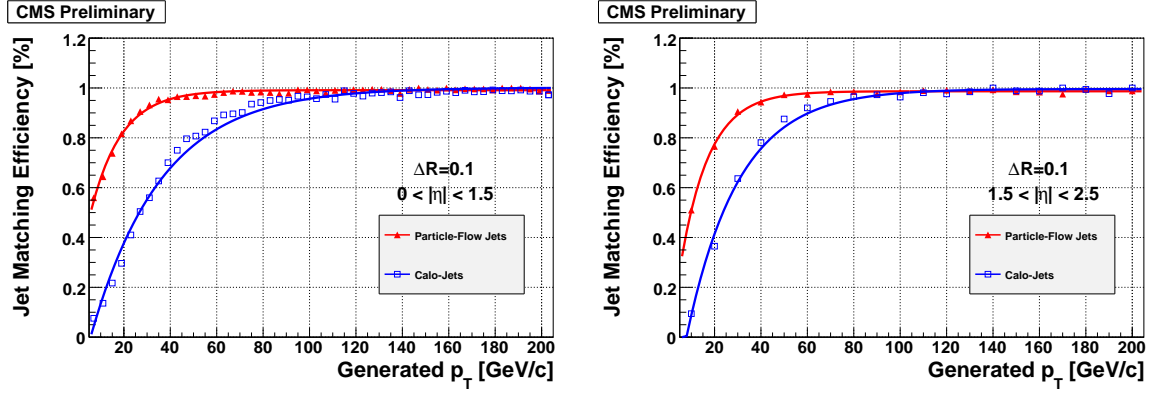


Figure 3.9.: The efficiency of PF jets, and Calo jets, matched to generated jets in the barrel region (left) and the endcap (right), taken from [7]. The superior performance of PF jets is evident because they are more efficiently matched to the generator, “truth” jets, at a lower p_T threshold: termed a shaper turn-on.

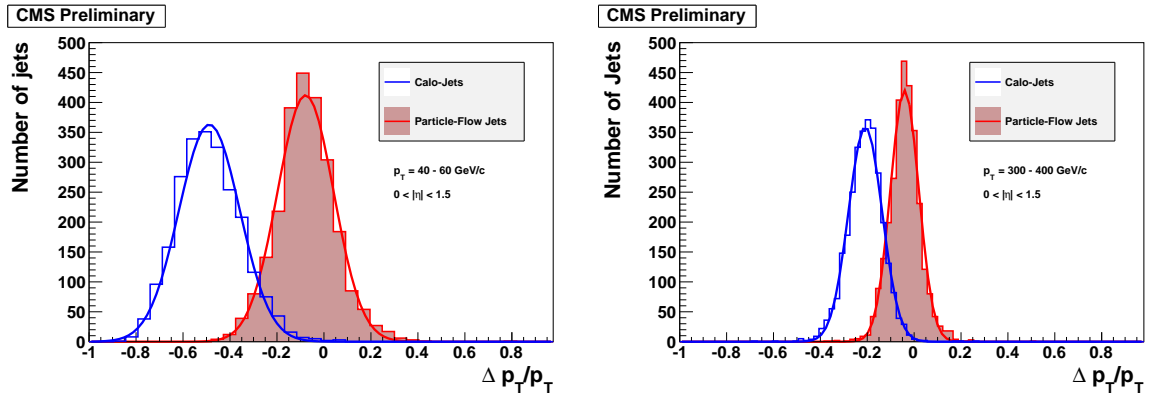


Figure 3.10.: The momentum resolution, $(p_T^{\text{rec}} - p_T^{\text{gen}})/p_T^{\text{gen}}$ of PF jets, and Calo jets, for low energy jets ($40 \text{ GeV} < p_T < 60 \text{ GeV}$) (left) and for high momentum jets ($300 \text{ GeV} < p_T < 400 \text{ GeV}$) (right) in the barrel region, taken from [7]. Not only are the peaks shaper for PF jets, meaning a smaller (and therefore better) overall momentum resolution, but it is also peaking much closer to zero, meaning the jet measurement is much closer to the generated jet momentum.

involving a large imbalance in transverse momentum as the weakly interacting Lightest Supersymmetric Partner (LSP) exits the detector. DM production would also lead to such a signature. Measurements of missing transverse energy and momentum are therefore crucial to the search for new physics at CMS, as they have been crucial in previous discoveries - for example of the W boson [8], and in searches for other processes [9, 10].

The missing transverse energy vector, \vec{E}_T^{miss} is formed by adding the transverse energy vectors $\sum \vec{E}_T$ of all the particles formed in an event. The missing transverse energy vector $\vec{E}_T^{\text{miss}} = -\sum \vec{E}_T$, where $|\vec{E}_T^{\text{miss}}| = E_T^{\text{miss}} = |\sum \vec{E}_T|$; ie, it is equal in magnitude and opposite in direction to the total visible energy in the event. In an analogous way to jets (and usually using such jets), E_T^{miss} can be built using various algorithms. Calorimeter (Calo) E_T^{miss} , in the same way as Calo jets, is built from calorimeter information alone while PF E_T^{miss} is calculated from all of the transverse energies of reconstructed particles in an event. Again, enhanced performance is seen using the PF algorithm over calorimeter information alone, see Figure 3.11. However the improvement is less marked, as energy measurements of the particle flow objects are driven by the calorimeter resolution. In the analysis presented in this thesis, PF E_T^{miss} is used, where any muons present have been removed from the calculation. It therefore mimics Calo E_T^{miss} , only with an enhanced resolution.

3.3.3. Muons

Muons are reconstructed using the muon system and the tracker, and the reconstruction algorithms use the concept of “regional reconstruction”. On the basis of an input or seed from the muon system, the software only reconstructs the part of the tracker from which the muon causing the seed could originate. This means that only a very small part (typically a few percent) of the tracker volume must be processed to reconstruct a muon; thereby speeding up the procedure and reducing the CPU power necessary to process an event.

Muon reconstruction has three stages: local, standalone and global reconstruction. Starting with a seed which defines a region of interest, which could be from the L1 seeds (from the RPCs) or from patterns of hits found in the CSCs and/or DT, a local reconstruction is performed in surrounding compatible muon chambers. The standalone reconstruction uses information from just the muon system; measurements of track position, momentum and direction of travel are taken, and extrapolated to the nominal interaction point. Global reconstruction then extends the resulting muon trajectories

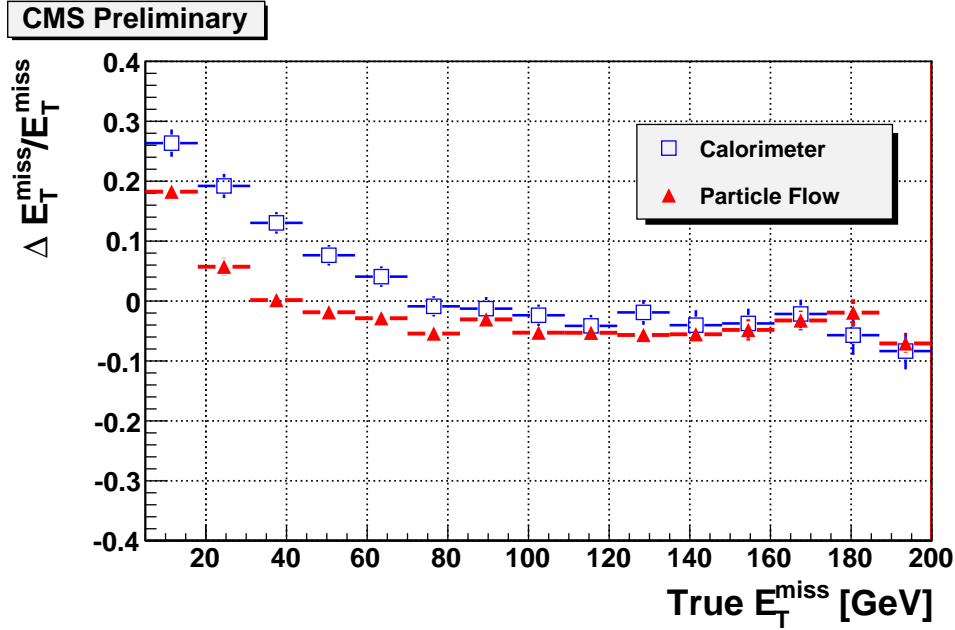


Figure 3.11.: The momentum resolution, $(E_{T,rec}^{\text{miss}} - E_{T,gen}^{\text{miss}})/E_{T,gen}^{\text{miss}}$ of PF and Calo E_T^{miss} , taken from [7]. An improved resolution is seen using the PF algorithm, particularly at low values of E_T^{miss} . At higher E_T^{miss} values, energy measurements are dominated by the calorimeter resolution and values using the two different methods converge.

to include hits in the silicon tracker. A track is extrapolated from the innermost muon chamber to the outer tracker surface, and compatible silicon layers determined. Candidates for the muon trajectory are built from pairs of hits in separate layers of the tracker and χ^2 of the fit is used to ensure a “good” muon candidate; to detect any bremsstrahlung or significant energy loss. High energy muons present particular difficulty as they suffer huge energy loss and severe electromagnetic showers in the muon system; the χ^2 probability of the fit compared to the the χ^2 probability of the tracker only trajectory allows accurate momentum reconstruction of such objects.

3.4. The Trigger

Crucial to the successful operation of CMS is the trigger. The pp interaction cross section is 100 mb, while for example, the W boson production cross section is some 6 orders of magnitude less than this, and the rare physics processes that CMS was built to search for, such as Higgs boson and SUSY production, many times smaller still; see Figure 3.12. The LHC delivers an unprecedented high instantaneous luminosity so that such rare physics processes occur, but this also implies that the vast majority of the collisions result in ‘uninteresting’ physics: namely QCD processes. It would be impossible to record the very high volumes of data that come out of CMS, some PB s^{-1} , and not useful to do so. Therefore, a very efficient method of recording those events that appear ‘interesting’ is necessary.

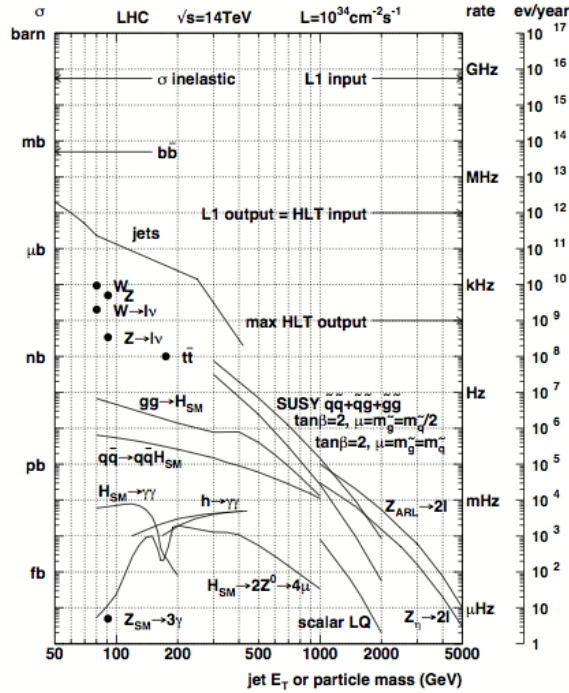


Figure 3.12.: Inclusive pp cross sections (σ) for basic and rarer physics processes, showing some of the phenomena on the physics programme at CMS. Shown on the right are the interaction rates for LHC design luminosity, $10^{34}\text{cm}^{-2}\text{s}^{-1}$. Taken from [11].

A two tier trigger system reduces the 40 MHz LHC bunch crossing rate to an output of 100 Hz, which is then saved offline to be reconstructed ready for physics analysis. The hardware based Level 1 Trigger (L1) uses fast algorithms with coarse inputs from the calorimeter and muon system to efficiently select, online (that is at the same rate as LHC

bunch crossings), those events that appear interesting, reducing the 40 MHz collision rate to 100 kHz. A software based Higher Level Trigger (HLT) running on the event filter PC farm at Point 5 takes the output of the L1 trigger and reduces it further to 100 Hz, using more sophisticated inputs and algorithms. Performance of the subdetectors and readiness to collect data, monitored by the Data Acquisition System (DAQ) system, is supervised by the trigger control system. Events passing HLT selection requirements are sent to the CERN Computing Centre where complex algorithms using all the information from the CMS detector are used to fully reconstruct the event. More information on the CMS trigger can be found in Ref. [11].

3.4.1. The L1 Trigger

Low granularity inputs from the calorimeter and muon system are used to quickly select possibly interesting events, based on predefined and programmable algorithms and criteria. Parts of the hardware are Field Programmable Gate Array (FPGA) based, allowing some flexibility in algorithms, while other parts are Application Specific Integrated Circuit (ASIC) based, with predefined criteria. Events are selected if they show signs of interesting physics; for example have jets, electrons/photons, or muons. Global quantities such as total transverse energy and total missing transverse energy are also used. In order to see if an event contains any of these physics objects above a pre-defined energy threshold or multiplicity, the L1 trigger is separated into the Calorimeter Trigger, which looks for jets, photons and electrons, and the Muon Trigger, which looks for muons. Global quantities are computed at the Global Trigger (GT) and combined with information from the Calorimeter and Muon triggers, and here a decision is made to keep or reject an event.

In the Calorimeter Trigger, information from the ECAL, HCAL and HF are combined. First, the calorimeter is split into different (geographical) regions, and electron, photon and jet finding algorithms run on the separate parts of the subdetectors at the Regional Calorimeter Trigger (RCT). Information from the different regions is then combined at the Global Calorimeter Trigger (GCT), where overlaps in the regions are dealt with. In the Muon Trigger, information from the DT, CSCs and RPCs are combined. Muon track finding algorithms are applied to data from the DT and CSCs at the Regional Muon Trigger (RMT), and the Global Muon Trigger (GMT) combines information from all of the three subdetectors to get an enhanced resolution. Inputs from the GCT and GMT

are then combined at the GT, where the decision to keep or discard an event is made. The architecture of the L1 trigger is shown in Figure 3.13.

There is an inbuilt latency of $3.2 \mu\text{s}$ in the L1 trigger, meaning that on the first bunch crossing, it takes up to $3.2 \mu\text{s}$ to transmit the necessary information, and make a decision. This is driven by the data storage available for information from the tracker and preshower detectors; they need so much data storage that it must be saved before a L1 accept decision, and subsequent event read out, can be made. The decisions on the rest of the bunch crossings follow at the rate of collisions, and the architecture is ready to accept another event every 25 ns.

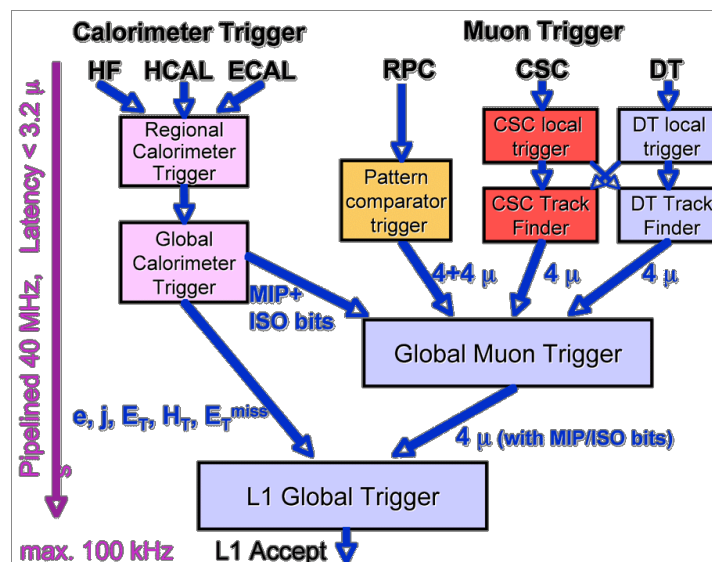


Figure 3.13.: Architecture of the L1 trigger. The calorimeter trigger takes inputs from the ECAL, HCAL and HF. The muon trigger takes inputs from the DT, CSCs and RPCs. A decision is made at the L1 GT, using inputs from the GCT and the GMT, of whether to pass an event onto the HLT or discard it.

A L1 accept decision is based upon the results of the various physics object reconstruction algorithms. Typically, every physics analysis has a type of event it is searching for; a particular topology. For example, the monojet analysis looks for events with a final state of one high p_T jet and large missing transverse energy. At L1, it requires events to pass the L1 seed L1_ETM36, L1_ETM40 or L1_ETM50, meaning the global variable, total missing transverse energy, must be above 36, 40 or 50 in L1 units of energy. A L1 trigger menu, comprised of all of the required L1 seeds for the whole physics programme at CMS, gives a certain bandwidth to each of the seeds. A low threshold seed will typically demand a large amount of bandwidth as more events are likely to be lower in energy, whereas a high threshold will require a lower bandwidth. Combined, the output to the

HLT of all of the L1 seeds in the trigger menu must not exceed 100 Hz, limited by the amount of data the HLT can process.

3.4.2. The High Level Trigger

When an event is accepted by the L1 trigger, the full detector information for that event (consisting of around 1 MB of data) is passed onto the HLT. On the event filter farm, which consists of over 1000 PC's, all of the detector information for each event is processed. Information not available at L1 becomes available. The additional computing power and longer time scales mean the full granularity of the calorimeter and tracker information (as well as L1 objects), can be used as inputs to more complex algorithms. As a result, much more stringent requirements are used to select events of interest, creating datasets which are used for offline analysis.

An analysis will typically use more than one HLT trigger, and similarly more than one analysis might use the same trigger (and an event pass more than one trigger). The mono-jet analysis, which searches for events which have one high momentum jet and large missing transverse energy, uses the triggers (or “paths”) `HLT_MET120_HBHENoiseCLEANED` and

`HLT_MONOCENTRALPFJET80_PFMETNoMu95_NHEF0p95`,

`HLT_MONOCENTRALPFJET80_PFMETNoMu105_NHEF0p95`. The first path requires the missing transverse energy of an event, calculated using calorimeter information only, to be greater than 120 GeV; in addition, this quantity is only formed from non-noisy parts of the calorimeter. The latter two paths are formed from events which have one jet, reconstructed using the PF algorithm [7], with transverse momentum above 80 GeV. Additionally, the missing transverse energy, calculated also with the PF algorithm without contributions from muons, must be above 95 or 105 GeV, and the neutral hadronic energy fraction of the jet must be less than 0.95. The combination of these three trigger paths allows events with a monojet topology to be selected efficiently; further kinematic and topological selections are applied offline to a dataset formed of events passing these trigger requirements. Similarly, every physics analysis uses a trigger (or triggers) suited to the topology under investigation.

In the same way that there is a L1 trigger menu, there is also a HLT menu comprised of all of the HLT trigger paths, and the bandwidths they require, which meets the needs of all of the physics analyses at CMS. The total bandwidth of the HLT menu must not exceed 100 Hz; or 100 events saved offline per second.

Chapter 4.

Jet Algorithms for the L1 Trigger Upgrade

4.0.3. ALGORITHMS FOR L1 JET RECONSTRUCTION

In this section we describe in detail the proposed algorithm to reconstruct, filter, and calibrate L1 jets. We assume that all L1 calorimetric information for a single event is available at the same time in the same place. This would be possible with the time multiplexed trigger approach (TMT) [?].

- **Jet Reconstruction**

The proposed jet algorithm builds jets from the outputs of the L1 calorimeter towers, thereby exploiting the full granularity of the CMS calorimeter. In the electromagnetic calorimeter (ECAL) one tower consists of 5×5 lead tungstate crystals and in the hadronic calorimeter one block of brass scintillator. In the centre of the detector, a tower covers a region of 0.087×0.087 in the $\eta - \phi$ plane with the η dimension increasing as η increases, see [?]. The ECAL and HCAL energy in each tower is summed and these 'L1CaloTowers' are the input to the algorithm.

A jet consisting of $n \times n$ towers is built at each tower site (See Figure 4.1); the algorithm is a sliding window across the calorimeter. Those jets with a non null energy are saved. The resulting numerous overlapping jets are sorted and filtered.

- **Tunable Parameters**

Jets are built from a flexible map of calorimeter towers; the jet shape and size can be set. Currently they can be circular or square, although there is scope for any desired shape. The size can be set to n towers. For circular jets this size represents

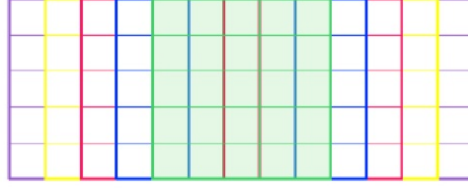


Figure 4.1.: Overlaps of 5×5 jet in 1D. A jet is built at each tower on the calorimeter

the length of the diameter, for square jets it represents the length of the side. In previous studies diameter 8 circular jets gave the best angular resolution, so these are presented here.

With the TMT it is technically possible to build two different L1 jet collections, of different parameters, at the same time, however this has not been investigated here.

• Jet Filtering

The jets are built from a sliding window across the calorimeter: a circular or square jet of $n \times n$ towers is 'seeded' at every tower. Therefore each tower contributes to $(2n - 1)$ separate, overlapping jets. These jets must be sorted and filtered to remove overlaps.

Firstly, all jets in each event are ordered in energy using a bitonic sort. This is a recursive parallel sorting algorithm suitable for implementation in hardware. It takes 2^N inputs and sorts in N steps using a series of bitonic sequences and splits.

However, there is often more than one overlapping jet of a particular energy. An asymmetry parameter in η and ϕ is also considered for each jet when this is the case:

$$A_{\eta,\phi} = \sum (\text{Constituent tower energies in positive } \eta, \phi) - \sum (\text{Constituent tower energies in negative } \eta, \phi) \quad (4.1)$$

A jet with all of its energy in the central tower will have $A_{\eta,\phi} = 0$ whereas a jet of the same energy with all energy deposits in an outer tower will have large $|A_{\eta,\phi}|$. If overlapping jets have the same energy, they are instead sorted to give the lowest asymmetry parameter. The first element in the sorted list is then the most energetic jet, with its energy concentrated most centrally within the $n \times n$ window.

The sorted list is then filtered to remove jets which overlap with this first jet. The process is repeated until 13 separate jets are found. This number is somewhat

arbitrary, chosen to be consistent with the current system. It is limited by hardware at some high number.

Jets are sorted initially in one dimension, along η or ϕ , and overlaps in one dimension are removed. The resulting list of the most energetic jets along or around the calorimeter is then sorted in the other direction to give the final jet collection.

- **Measurement of Pile-Up contribution**

The measurement of the PU contribution to the jet energy is evaluated event by event using a method inspired by the paper of Cacciari and Salam [?] and already used to correct offline jets. In a pp collision with a large number of overlapping proton-proton interactions, a large number of (relatively soft) jets originate from PU and are distributed evenly across the calorimeter. The median jet energy is therefore very likely to come from PU. Its energy density is a good estimator of the energy released by PU per unit of area in that event.

PU energy is uniform across the calorimeter, so it is simply subtracted from all jets in an event using

$$\rho = \frac{\text{median jet energy}}{A_{L1}} \quad (4.2)$$

$$\text{PU corrected } p_T = p_T - \rho \times A_{L1} \quad (4.3)$$

where A_{L1} is the area of the L1 jet.

In the following we show the effect of PU subtraction in the measurement of the jet energy. The same quantity could also be used to correct the isolation variables for electrons and muons and the H/E variable used to identify electrons at L1.

- **Calibration**

The raw jet energies from the calorimeter towers must be corrected to the jet energy scale. Different regions of the calorimeter give different responses so a set of calibration constants in P_T and η must be derived: so-called "L2L3 corrections". A non linear regression method is used on an independent subsection of 20,000 events of Single Muon 2012C data to provide a table of calibration constants.

Firstly, L1 ρ , the median jet energy per unit area in an event, is compared to ρ calculated offline and a set of calibration factors for L1 ρ are obtained. Raw jet energies are then subtracted for PU with the corrected ρ . Only jets with a positive energy are kept. L1 jets are calibrated to the offline L2L3 corrected AK5 calo jets (ie. they have also been PU subtracted). The leading offline jet in each event is

matched to a L1 jet within a cone of $\Delta R = 0.5$. L1 P_T , L1 η , offline P_T and offline η are inputs to a multivariant analysis [?]. This is trained to provide a lookup table of multiplication factors binned in L1 η and P_T . A calibration independent of PU is then achieved.

4.0.4. UPGRADE L1 JET ALGORITHM PERFORMANCE

Jet performance can be characterised by angular and energy resolutions, efficiencies and rates. 8×8 circular jets were simulated using high PU Zero Bias data taken in Run 2012C. The run studied had an average of 45 primary vertices per bunch crossing.

ANGULAR AND ENERGY RESOLUTIONS

Resolutions are measured as compared to offline ak5 calo jets. The leading ak5 calo jet (which must have $p_T > 20\text{GeV}$) is matched to a L1 jet within $\Delta R < 0.5$, and the resolutions are defined as:

$$\Delta_\eta = \eta_{AK5Calo} - \eta_{L1} \quad (4.4)$$

$$\Delta_\phi = \phi_{AK5Calo} - \phi_{L1} \quad (4.5)$$

$$\Delta_{p_T} = \frac{p_T - p_{T,AK5Calo}}{p_{T,AK5Calo}} \quad (4.6)$$

$$(4.7)$$

Angular and energy resolutions of the proposed upgrade algorithm compared to the current system are shown in Figure 4.2. There is a much improved angular resolution as the upgrade jets take advantage of the full granularity of the calorimeter. In high PU data, the energy resolution is improved due to the PU subtraction. In the current system, the leading offline jet has been matched to low energy PU jets, making the p_T resolution negative and giving the distribution a significant negative tail.

EFFICIENCIES

We measure the trigger turn on curves of L1 jet reconstruction. If the leading L1 jet in each event above a certain energy threshold is matched to an offline ak5 calo jet, the energy spectrum of the matched offline jet is plotted. All matched offline jet energies

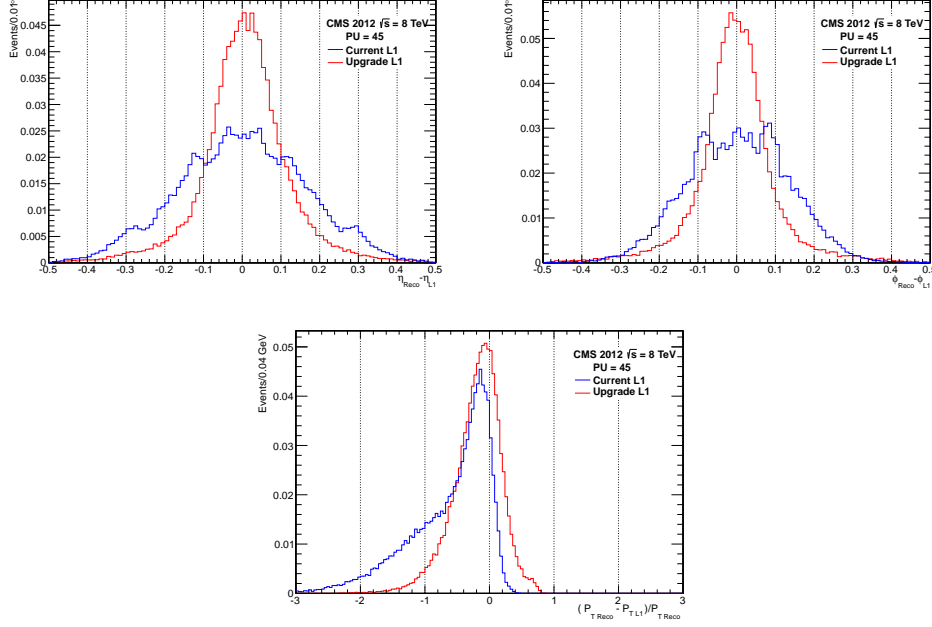


Figure 4.2.: Resolution of η , ϕ and p_T for 45 PU ZeroBias data taken in run 2012C. There is a clear improvement with the upgrade jets, plotted in blue.

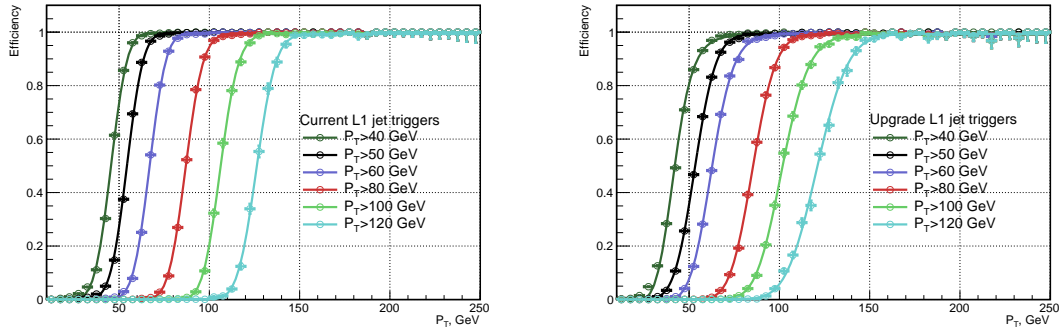


Figure 4.3.: On the left are the trigger turn on curves for the current jet algorithm and on the right are the trigger turn on curves for the upgrade jet algorithm, for various single jet trigger thresholds. These turn on curves were calculated using Single Muon 2012C data in PU normal PU conditions for 2012C running, 20 primary vertices per event.

are also plotted. By taking the difference between these two spectrums we attain trigger turn on curves, shown in Figure 4.3.

To attain sufficient statistics for the turn on curves, the upgrade jet algorithm was run on data taken in run 2012C with a L1 Single Muon trigger.

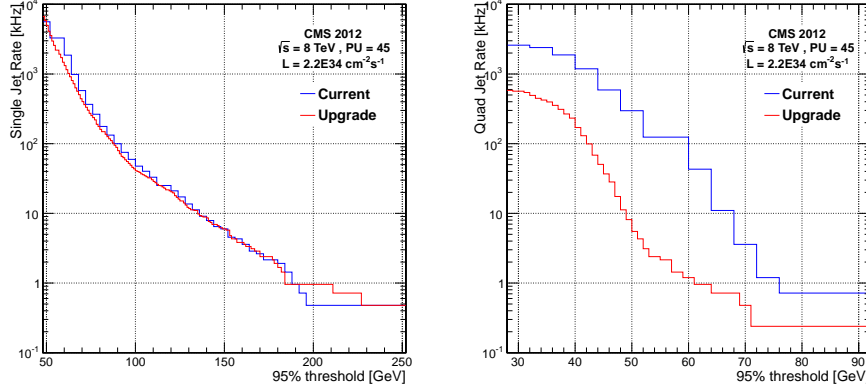


Figure 4.4.: Rates of single and quad jet triggers. The single jet trigger shows similar performance to the current system, while the multi-jet trigger show a large reduction in rate

RATES

The L1 trigger is limited to the number events it can pass to the HLT. Triggers can only take a certain bandwidth; the sum of all trigger rates must be ~ 300 kHz. In Zero Bias data, the rate at which the trigger would fire at a given L1 jet energy is calculated for a instantaneous luminosity scenario using the equation

$$\text{Rate}_{\text{Inst. lumi}} = \text{Rate}_{\text{event}} \cdot \frac{L \times \sigma_{pp}}{PU} \quad (4.8)$$

Where L is the instantaneous luminosity, σ_{pp} is the proton-proton cross section and PU is the number of vertices per bunch crossing.

Rates are plotted in terms of the 95% threshold: physics groups set the cuts in analyses dependant on offline values at which trigger rates are $\geq 95\%$ efficient. Taking a set of turn on curves, such as those in Figure 4.3, a linear conversion function between L1 threshold and 95% threshold is attained. Figure 4.4 shows the single and quad jet trigger rates. The current and upgrade single jet rates are comparable, as the PU subtraction does very little to the leading jet in the event, whereas the multi jet triggers such as the quad jet trigger sees a significant reduction in rate as PU jets are removed from the event.

Chapter 5.

Searching for Compressed SUSY with monojet events

“There, sir! that is the perfection of vessels!”

— Jules Verne, 1828–1905

5.1. Analysis

cp PAS.tex .

Appendix A.

Pointless extras

« *Le savant n'étudie pas la nature parce que cela est utile;
il l'étudie parce qu'il y prend plaisir,
et il y prend plaisir parce qu'elle est belle.* »
— Henri Poincaré, 1854–1912

Appendixes (or should that be “appendices”?) make you look really clever, 'cos it's like you had more clever stuff to say than could be fitted into the main bit of your thesis. Yeah. So everyone should have at least three of them...

A.1. Like, duh

Padding? What do you mean?

A.2. $y = \alpha x^2$

See, maths in titles automatically goes bold where it should (and check the table of contents: it *isn't* bold there!) Check the source: nothing needs to be specified to make this work. Thanks to Donald Arsenau for the teeny hack that makes this work.

Bibliography

- [1] K. Aamodt, et al., The ALICE experiment at the CERN LHC, JINST 3 (2008) S08002. [doi:10.1088/1748-0221/3/08/S08002](#).
- [2] G. Aad, et al., The ATLAS Experiment at the CERN Large Hadron Collider, JINST 3 (2008) S08003. [doi:10.1088/1748-0221/3/08/S08003](#).
- [3] S. Chatrchyan, et al., The CMS experiment at the CERN LHC, JINST 3 (2008) S08004. [doi:10.1088/1748-0221/3/08/S08004](#).
- [4] J. Alves, A. Augusto, et al., The LHCb Detector at the LHC, JINST 3 (2008) S08005. [doi:10.1088/1748-0221/3/08/S08005](#).
- [5] S. Chatrchyan, et al., CMS Physics: Technical Design Report Volume 1: Detector Performance and Software.
- [6] M. Cacciari, G. P. Salam, G. Soyez, The anti- k_t jet clustering algorithm, JHEP 04 (2008) 063. [arXiv:0802.1189](#), [doi:10.1088/1126-6708/2008/04/063](#).
- [7] CMS Collaboration, [Particle flow event reconstruction in cms and performance for jets, taus and met](#), CMS Physics Analysis Summary CMS-PAS-PFT-09-001 (2009). URL <http://cdsweb.cern.ch/record/1194487>
- [8] G. Arnison, et al., Experimental observation of isolated large transverse energy electrons with associated missing energy at $\sqrt{s} = 540$ GeV, Phys. Lett. B 122 (1983) 103–116. [doi:10.1016/0370-2693\(83\)91177-2](#).
- [9] C. Albajar, et al., Events with large missing transverse energy at the CERN collider: I. $W \rightarrow \tau\nu$ decay and test of $\tau - \mu - e$ universality at $Q^2 = m_W^2$, Phys. Lett. B 185 (1986) 233–240. [doi:10.1016/0370-2693\(87\)91561-9](#).
- [10] C. Albajar, et al., Events with large missing transverse energy at the CERN collider: II. Search for the decays of W^{\pm} into heavy leptons and of Z^0 into non-interacting particles, Phys. Lett. B 185 (1986) 241–248. [doi:10.1016/0370-2693\(87\)91562-0](#).

-
- [11] S. Cittolin, A. Rcz, P. Sphicas, CMS The TriDAS Project: Technical Design Report, Volume 2: Data Acquisition and High-Level Trigger. CMS trigger and data-acquisition project, Tech. rep., Geneva (2002).

List of Figures

3.1. The LHC accelerator ring, showing the locations of the four main experiments at the four collision points.	6
3.2. The CMS detector, with the main subsystems labelled.	8
3.3. The CMS tracker, shown in the rz plane. The pixel detector is shown at the centre of the tracker, closest to the interaction region (shown by the black dot), and the strip detector surrounds it. The different subsystems of the strip detector are shown, taken from Ref.[3].	10
3.4. Geometric view of the CMS ECAL. Barrel crystals are arranged in modules and supermodules, and endcap crystals arranged in supercrystals. Also shown is the preshower detector.	11
3.5. Longitudinal view of the CMS HCAL. Locations of the HB, HO, HE and HF are shown with values of η . The purple regions represent the muon detectors which further restrict the volume of the HO.	12
3.6. Muon transverse momentum resolution, shown as a function of muon p_T in the barrel (left) and the endcaps (right). The resolution of the tracker and muon system is shown, and the enhancement gained by combining the information.	14
3.7. A slice of the CMS detector is shown, with various particles, or physics objects, traversing it. By combining information from each of the subdetectors, each of the particles produced in an event can be identified and the whole event reconstructed.	15

- 3.8. The relative insensitivity of the anti- k_T algorithm to PU is shown, compared to other common jet algorithms. The distribution of back reaction, corresponding to the net change in p_T to each of the two hardest jets (where each jet has $p_T > 200$ GeV), when adding $PU \sim 25$ to the event, corresponding to LHC running conditions in the next phase of data taking starting in 2015. Taken from[6]. 16
- 3.9. The efficiency of PF jets, and Calo jets, matched to generated jets in the barrel region (left) and the endcap (right), taken from[7]. The superior performance of PF jets is evident because they are more efficiently matched to the generator, “truth” jets, at a lower p_T threshold: termed a shaper turn-on. 18
- 3.10. The momentum resolution, $(p_T^{\text{rec}} - p_T^{\text{gen}})/p_T^{\text{gen}}$ of PF jets, and Calo jets, for low energy jets ($40 \text{ GeV} < p_T < 60 \text{ GeV}$) (left) and for high momentum jets ($300 \text{ GeV} < p_T < 400 \text{ GeV}$) (right) in the barrel region, taken from[7]. Not only are the peaks shaper for PF jets, meaning a smaller (and therefore better) overall momentum resolution, but it is also peaking much closer to zero, meaning the jet measurement is much closer to the generated jet momentum. 18
- 3.11. The momentum resolution, $(E_{T,\text{rec}}^{\text{miss}} - E_{T,\text{gen}}^{\text{miss}})/E_{T,\text{gen}}^{\text{miss}}$ of PF and Calo E_T^{miss} , taken from[7]. An improved resolution is seen using the PF algorithm, particularly at low values of E_T^{miss} . At higher E_T^{miss} values, energy measurements are dominated by the calorimeter resolution and values using the two different methods converge. 20
- 3.12. Inclusive pp cross sections (σ) for basic and rarer physics processes, showing some of the phenomena on the physics programme at CMS. Shown on the right are the interaction rates for LHC design luminosity, $10^{34} \text{cm}^{-2} \text{s}^{-1}$. Taken from[11]. 21
- 3.13. Architecture of the L1 trigger. The calorimeter trigger takes inputs from the ECAL, HCAL and HF. The muon trigger takes inputs from the DT, CSCs and RPCs. A decision is made at the L1 GT, using inputs from the GCT and the GMT, of whether to pass an event onto the HLT or discard it. 23
- 4.1. Overlaps of 5×5 jet in 1D. A jet is built at each tower on the calorimeter 26

-
- 4.2. Resolution of η , ϕ and p_T for 45 PU ZeroBias data taken in run 2012C. There is a clear improvement with the upgrade jets, plotted in blue. . . . 29
- 4.3. On the left are the trigger turn on curves for the current jet algorithm and on the right are the trigger turn on curves for the upgrade jet algorithm, for various single jet trigger thresholds. These turn on curves were calculated using Single Muon 2012C data in PU normal PU conditions for 2012C running, 20 primary vertices per event. 29
- 4.4. Rates of single and quad jet triggers. The single jet trigger shows similar performance to the current system, while the multi-jet trigger show a large reduction in rate 30

List of Tables

1. Acronyms

ALICE	A Large Ion Collider Experiment
ATLAS	A Toroidal LHC ApparatuS
APD	Avalanche Photo-Diode
ASIC	Application Specific Integrated Circuit
BSM	Beyond Standard Model
CERN	European Organisation for Nuclear Research
CMS	Compact Muon Solenoid
CMSSM	Compressed Minimal SuperSymmetric Model
CSCs	Cathode Stripe Chambers
CSV	Combined Secondary Vertex
CSVM	Combined Secondary Vertex Medium Working Point
DAQ	Data Acquisition System
DM	Dark Matter
DT	Drift Tube
ECAL	Electromagnetic Calorimeter
EB	Electromagnetic Calorimeter Barrel
EE	Electromagnetic Calorimeter Endcap

ES	Electromagnetic Calorimeter pre-Shower
EMG	Exponentially Modified Gaussian
EPJC	European Physical Journal C
EWK	Electroweak Sector
FPGA	Field Programmable Gate Array
GCT	Global Calorimeter Trigger
GMT	Global Muon Trigger
GT	Global Trigger
HB	Hadron Barrel
HCAL	Hadronic Calorimeter
HE	Hadron Endcaps
HF	Hadron Forward
HLT	Higher Level Trigger
HO	Hadron Outer
HPD	Hybrid Photodetectors
ISR	Initial State Radiation
LUT	Look Up Table
L1	Level 1 Trigger
LEP	Large Electron-Positron Collider
LHC	Large Hadron Collider
LHCb	Large Hadron Collider Beauty
LO	Leading Order
LSP	Lightest Supersymmetric Partner
MC	Monte Carlo
NLL	Next to Leading Logarithmic Order

NLO	Next to Leading Order
NNLO	Next to Next Leading Order
PF	Particle Flow
POGs	Physics Object Groups
PS	Proton Synchrotron
PU	pile-up
QED	Quantum Electro-Dynamics
QCD	Quantum Chromo-Dynamics
QFT	Quantum Field Theory
RBXs	Readout Boxes
RPCs	Resistive Plate Chambers
RCT	Regional Calorimeter Trigger
RMT	Regional Muon Trigger
SUSY	SUperSYmmetry
SM	Standard Model
SMS	Simplified Model Spectra
SPS	Super Proton Synchrotron
TIB	Tracker Inner Barrel
TEC	Tracker Endcaps
TID	Tracker Inner Disks
TOB	Tracker Outer Barrel
TF	Transfer Factor
TP	Trigger Primitive
VEV	Vacuum Expectation Value
VPT	Vacuum Photo-Triode

WIMP Weakly Interacting Massive Particle